Original Manuscript

Journal of Vibration and Control
2023, Vol. 0(0) 1–15

DOI: 10.1177/10775463231182256
journals.sagepub.com/home/jvc
Sage

Passive control on deep cavity noise at subsonic speeds by leading-edge grooves

Weishuang Lu[1] and Guannan Zheng[1,2]

Abstract

Control effects of leading-edge grooves on deep cavity noise are investigated numerically. The length-to-depth ratio of the grooves are 0.5, 1, and 4, respectively. The freestream Mach number is equal to 0.16, corresponding to the Re based on the cavity length of 7.7×10^5. The Detached Eddy Simulations (DES) combined with Ffowcs Williams–Hawkings (FW-H) acoustic analogy are adopted to simulate the characteristic information of the flow field and the acoustic field. The analysis results show that all grooves investigated in this paper have a certain noise control effect, and the groove with the most obvious noise reduction effect is the groove with a length-to-depth ratio of 0.5, namely, the deep groove. Narrowband noise generated by the flow-acoustic feedback (100–700 Hz) and the acoustic resonance mechanism (above 300 Hz) and broadband noise caused by the turbulent disturbance in the shear layer of the cavity mouth significantly reduce when the deep groove is used for the noise control. The reason for the noise reduction is that the leading-edge grooves can effectively change the flow characteristics near the mouth of the downstream cavity. When the flow passes the grooves, the groove flow reduces the energy in the fluid, resulting in the significant decrease of flow velocity of the boundary layer of the incoming flow of the cavity. In addition, the use of the deep groove also promotes the vortex concentration position to move towards the bottom of the cavity, pushes the energy in the shear layer of the downstream cavity towards the front-edge as well as the bottom of the cavity, and stabilizes the development of the shear layer near the cavity mouth.

Keywords

cavity noise, noise reduction, passive control, flow-acoustic feedback, acoustic resonance

1. Introduction

Cavity structures, such as slat cove (Chen et al., 2021; Dobrzynski W, 2010), pin holes (Abdelmwgoud et al., 2020), landing gear bays (Pereira et al., 2021; Zhao K et al., 2020), and landing gear well (Casalino et al., 2014), are major noise sources during aircraft takeoff and landing (Pott-Pollenske et al., 2002). When the flow passes the cavity, the shear layer will impinge on the rear wall and produce intense oscillation and noise radiation. Due to their necessary existence on aircraft, the problem of flow over the cavities has inspired a large volume of research work, both experimental and computational, over the past several decades. The research results (Rockwell and Naudascher, 1978) show that, under certain conditions, the cavity flow is unsteady and self-sustained oscillation occurs. For rigid-wall deep cavities (length-to-depth ratio, L/D <1), the generation mechanism of the narrowband noise in the cavity noise can be classified into two types. One is the fluid-dynamic oscillation caused by the instability of the cavity shear layer and are enhanced through an acoustic-wave feedback mechanism, also called flow-acoustic feedback. The empirical formula proposed by Rossiter (1964) is still widely used to match the frequency of the narrowband noise, which depends on the freestream velocity, the vortex convection speed (East, 1966), and the phase delay (Larcheveque et al., 2003). The other is the acoustic resonance caused by the fluid-resonant mechanism due to the standing wave inside the cavity. The frequency of acoustic resonance noise is related to the geometry of the cavity and sound speed, and almost independent of the flow velocity (Mendoza, 1997).

There are many control techniques proposed to suppress the cavity noise, whether active or passive, depending on the external energy input (Li et al., 2013). Passive control

[1]Institute of Mechanics, Chinese Academy of Sciences, Beijing, China
[2]School of Engineering, University of Chinese Academy of Sciences, Beijing, China

Received: 16 March 2023; revised: 23 May 2023; accepted: 29 May 2023

Corresponding author:
Guannan Zheng, Institute of Mechanics, Chinese Academy of Sciences, Beijing, China; School of Engineering, University of Chinese Academy of Sciences, NO.15 Beisihuanxi Road, Haidian District, Beijing 100190, China.
Email: zhengguannan@imech.ac.cn

techniques do not involve any external energy input and just require geometric modifications or wall material replacements. Common passive noise reduction methods for cavities include leading-edge spoilers, wall perforated panels, changes in geometric shapes of front and rear wall, etc. Chaudhari and Raman (2011) experimentally investigated cavity tone suppression mechanism by placing a cylinder in cross flow. This control method can effectively reduce tonal amplitudes of the near-field noise in the cavity. Lawson and Barakos (2009) numerically simulated flow noise characteristics of a cylinder placed horizontally above the front-edge of a cavity. The numerical results indicate that the horizontally placed cylinder can not only weaken the interaction of flow structures with rear-edge solid walls and delay the instability of the shear layer, but also raise the height of the shear layer, suppressing pressure pulsations generated by the rear-edge walls from propagating into the far field as sound waves. Wang et al. (2016) numerically investigated the passive control of cavity flow oscillations by a dimpled non-smooth surface, noticing that the cavity noise intensity caused by a turbulent boundary layer is weaker than that of a laminar boundary layer. Saddington et al. (2016) studied different passive control techniques experimentally, including spoilers, porous walls, leading-edge wedges, and the leading-edge deep cavity. His test results show that leading-edge control techniques are more effective on suppressing cavity tone amplitudes than trailing-edge modifications.

Some effective noise reduction methods are summarized above. However, these research work is basically carried out based on the shallow cavity models (L/D >1), and less attention has been paid to deep cavities (Guo et al., 2021). The mechanisms of noise reduction by flow past shallow and deep cavities are different. In shallow cavities, there is almost no acoustic resonance noise mechanism, but in deep cavities, this is the dominant noise mechanism.

It should be noted that the cavity itself may also be designed as a leading-edge noise control device. The flow over the leading-edge cavity and the deep cavity successively can be regarded as flow over tandem cavities. However, the tandem cavities refer to two cavities of comparable size, whereas the leading-edge cavity for noise control is much smaller in size than the downstream cavity. Currently, there have been some studies on flow over tandem cavities. Wang et al. (2020) analyzed the acoustic-driven flow interactions between tandem deep cavities using a proper orthogonal decomposition (POD) method. Zhang and Edwards (1992, 1999) and Taborda et al. (2001) measured supersonic and transonic flows over tandem cavities, respectively. According to their work, the downstream deep cavity is shown to be significantly affected by the presence of an upstream cavity, and the effect of the upstream shallow cavity is more obvious than that of upstream deep cavity. These findings all suggest that the upstream cavity has a strong influence on the flow characteristics of the downstream cavity, and the geometry of the upstream cavity is also an important influencing factor.

Accordingly, the aim of this paper is to investigate numerically the noise reduction effect of leading-edge cavities with different length-to-depth ratios on a deep cavity at a Ma = 0.16. To facilitate the distinction between the leading-edge cavity and the downstream deep cavity, the leading-edge cavity is referred to as a groove in this paper. The ratios of length over depth of the grooves are 0.5, 1, and 4, respectively. The ratio of length-to-depth ratio of the deep cavity is 2/3. The Detached Eddy Simulations (DES) combined with Ffowcs Williams–Hawkings (FW-H) acoustic analogy are adopted to simulate the flow and noise characteristics of the cavities. DES is used to compute the acoustic source while the FW-H acoustic analogy is employed for the prediction of the far-field sound.

2. Computational setup

2.1. Cavity models

The model studied in this paper is a three-dimensional rectangular cavity configuration at the rear of rectangular grooves with different length-to-depth ratios, as shown in Figure 1, where the positive x axis refers to the stream-wise direction, the y axis is perpendicular to the wall, and z axis refers to the span-wise direction. Geometrical parameters of the cavity and the grooves are shown in Table 1, where L is the length, D is the depth, W is the width, the subscript c represents the parameters of the cavity, and the subscript g represents the parameters of the grooves. ΔL is the distance between the cavity and the groove, which is 40 mm in this paper.

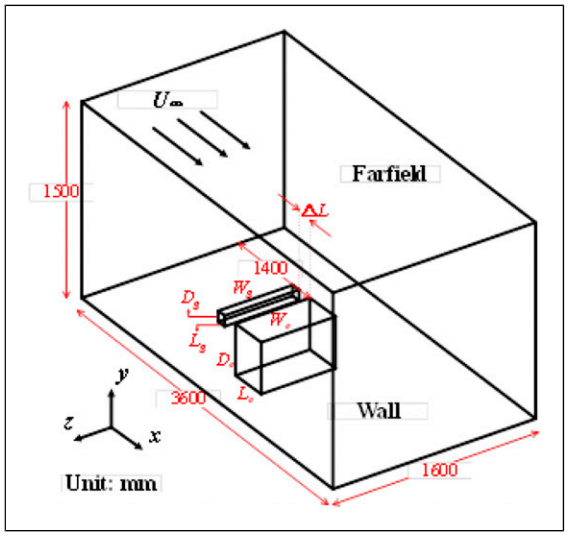

Figure 1. Schematic diagram of computational domain.

To facilitate the verification of the reliability of the simulation method, the length (L_c) of the cavity for the Base case is 200 mm, the width (W_c) is 600 mm, and the depth (D_c) is 300 mm, the distance from the front-edge of the cavity to the inlet is 1400 mm, which are consistent with the parameters of Guo et al., 2021 studies model.

2.2. Computational methods

In this paper, the 3D structured grid is created by the mesh generation software ANSYS ICEM. The computational domain selected in this paper is shown in Figure 1. Its length, width, and height are set to $L \times W \times H = 3600$ mm $\times$ 1600 mm $\times$ 1500 mm. There are three types of mesh with small, medium, and large grid numbers, namely, coarse, medium, and fine mesh, respectively. The total numbers of cells are 2.1 million, 4.3 million, and 7.6 million, respectively. The details of these three computational grids are shown in Table 2.

A commercial CFD solver ANSYS FLUENT 2021 was used to simulate the flow field and acoustic field. The gas properties are chosen as ideal-gas. The inlet, outlet, two sides, and above of the computational domain are all set to pressure-far-field boundary condition. The freestream Mach number is equal to 0.16. The temperature and pressure are consistent with the experimental environment of Guo et al., 2021 work: $T_\infty = 303$ K and $P_\infty = 101325$ Pa. No-slip solid-wall boundary conditions are applied on the walls inside the cavity and groove, as well as the bottom of the computational domain, as shown in Figure 1.

A k-ε two-equation model is used to calculate the steady-state flow field. The momentum and turbulent kinetic energy in the equation are two-order upwind schemes. The pressure–velocity coupling is dealt with the SIMPLE algorithm. The calculation result of the steady-state flow field is used as the initial value of the transient calculation, and the DES (Detached Eddy Simulation, also named as hybrid LES/RANSs) method is used to calculate the transient flow field to obtain acoustic sources. The RANS model is the Spalart–Allmaras model, whereas the subgrid-scale model of LES is wall-adapting local eddy-viscosity. The time step is set to $\Delta t = 2 \times 10^{-5}$ to ensure the Courant–Friedrichs–Lewy number which is less than 1.

A Ffowcs Williams–Hawkings (FW-H) acoustic analogy is employed to calculate the acoustic field. To analyze sound pressure information of the cavity noise, a surface pressure monitoring point is placed on cavity bottom in the spanwise centerline, namely, S1. 5 far-field pressure monitoring points (F1-F5) are arranged at the flyover direction (x–y plane) 2 m away from the front-edge of the cavity, as shown in Figure 2. The direction angles of these far-field pressure monitoring points are 75°, 90°, 115°, 120°, and 135°, respectively. The total duration of the cavity noise calculation is 1.5 s. The noise calculation time is divided into 15 parts, each part is 0.1 s, and the analysis frequency interval is 10.10 Hz. Afterwards, by performing fast Fourier transform (FFT) on each part of the noise data, and then averaging the results of each part a relatively smooth noise power spectrum result can be obtained.

To deeply explore the noise reduction mechanism as well as the flow mechanism, velocity distributions in boundary layers and shear layers are selected for further analysis. The locations of the boundary/shear layer are shown in Figure 3

2.3. Model validation and grid independence

To verify the reliability of the numerical model and grid independence, the numerical simulation results about the power spectral density (PSD) of the near-field noise and far-field noise intensity are compared with those of wind tunnel

Table 1. Geometrical parameters of cases in this paper (unit: mm).

	L_c	D_c	$W_c = W_g$	L_g	D_g	ΔL
Base	200	300	600	—	—	—
Case1	200	300	600	20	40	40
Case2	200	300	600	20	20	40
Case3	200	300	600	20	5	40

Table 2. Details of the computational grids.

	$N_x \times N_y \times N_z$	Quantity (Million)	First cell height
Coarse	220 × 60 × 160	2.1	$2 \times 10^{-3} L_c$
Medium	280 × 80 × 190	4.3	$1 \times 10^{-3} L_c$
Fine	330 × 110 × 210	7.6	$5 \times 10^{-4} L_c$

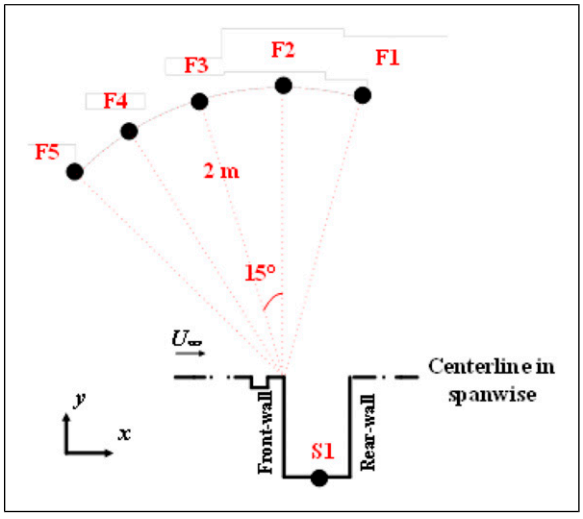

Figure 2. Locations of surface (S1) and far-field (F1–F4) microphones.

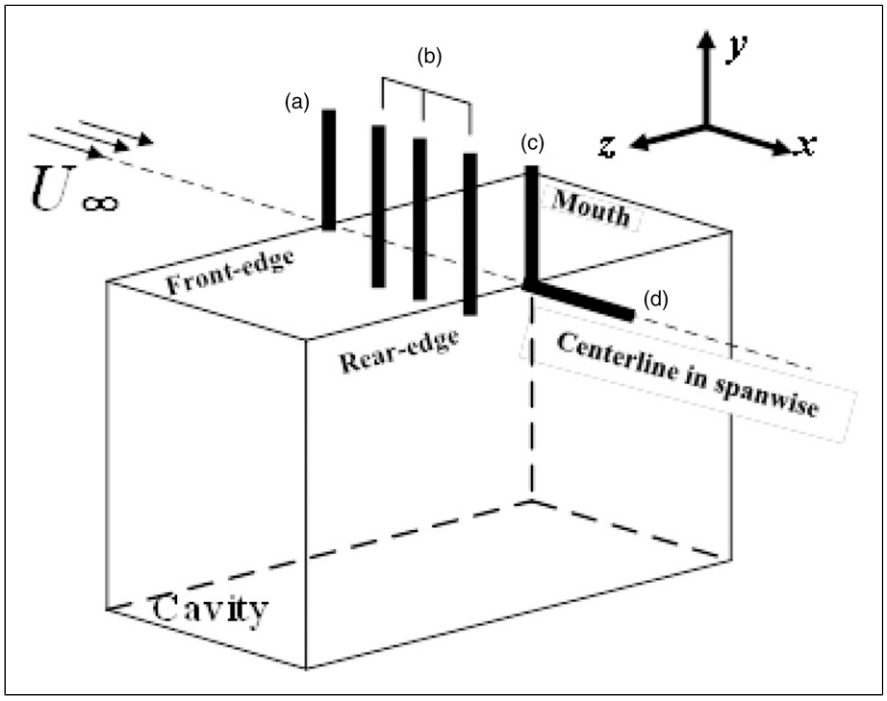

Figure 3. Location of the analyzed boundary/shear layer (a) boundary layer at the front-edge of the cavity mouth; (b) shear layers at x = 0.25 L, 0.5 L and 0.75 L; (c) boundary layer at the rear-edge of the cavity mouth; (d) wall at the rear-edge of the cavity.

test results (Guo et al., 2021). The numerical verifications about an acoustic field were performed on the Base case at $Ma = 0.16$.

Figure 4 shows the power spectral density (PSD) of the near-field noise calculated by three computational grids. Referring to the experimental results measured by Guo et al. (2021), coarse mesh resolution has a large calculation error in a high-frequency band. When the resolution of the coarse grid is increased to the medium grid and the fine grid level, the numerical simulation results of broadband noise intensity are almost in agreement with the experimental results. In addition, as it can be seen from the experimental result in Figure 4, there are several narrowband noises superimposed on the broadband spectrum, among which the narrowband noise characterized by the frequency of 244 Hz is the strongest and is regarded as the dominant tone. All numerical simulation results basically reproduce the frequencies corresponding to these narrowband noises, and the errors of the intensity of the dominant tone are less than 3%.

In order to further verify the reliability of the numerical model and grid independence, the comparison of far-flied noise intensity of the dominant tone between experimental results and numerical simulation results are presented in Figure 5. The variation trend of the far-flied noise intensity of the dominant tone is well simulated by the three grids. The simulation results of the fine grid and medium grid almost coincide with each other, and the intensity difference between the experimental results and these simulations is less than 2.5 dB with an error of 3%.

According to the analysis above, there is little error between the results of medium and fine grid resolution. Therefore, on the premise of the calculation accuracy and the limited computing resources, the grids in the subsequent numerical calculation are generated according to the setting of the medium grid.

3. Frequency prediction formula of cavity noise

3.1. Flow-acoustic feedback

When fluid flow passes the front-edge of the cavity, it separates and forms a shear layer due to Kelvin–Helmholtz instability, which leads to disturbance. During the downstream excursion of the flow, the disturbance is magnified continuously in the shear layer. When the flow is reattached to the rear-edge wall of the cavity, the impact with the rear-edge solid wall stimulates a new disturbance, which propagates to the upstream shear layer in the form of sound waves, and causes new shear layer instability, thus forming a feedback loop.

From an acoustic point of view, Rossiter J. (1964) summarizes the phenomenon of flow-acoustic feedback as an acoustic feedback model, and the characteristic frequencies can be predicted using a semi-empirical formula, as shown in equation (1).

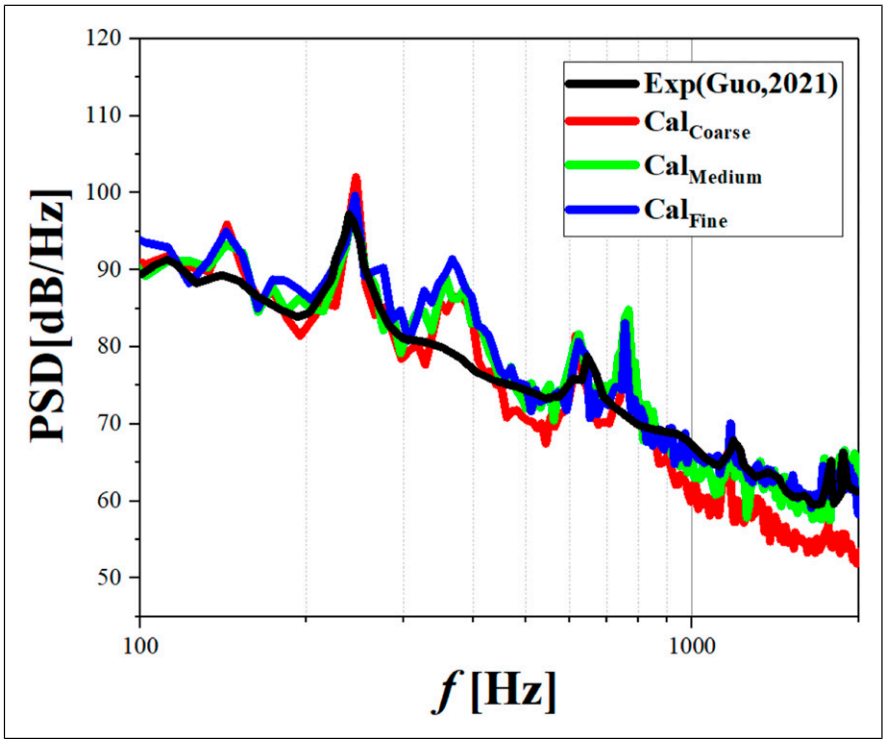

Figure 4. Comparison of power spectral density (PSD) of the near-field noise between experimental results and numerical simulation results calculated by three computational grids.

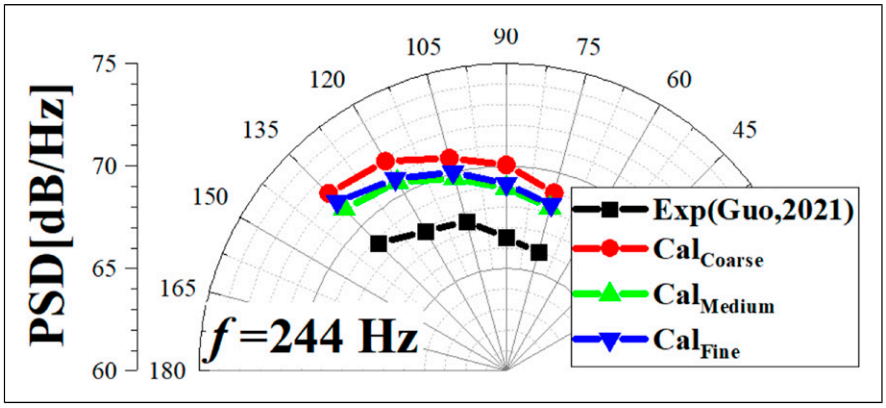

Figure 5. Comparison of far-flied noise intensity of dominant tone between experimental results and numerical simulation results calculated by three computational grids.

$$f_n = \frac{U_\infty}{L} \cdot \frac{n - \alpha}{1/\kappa + Ma} \tag{1}$$

where f_n is the characteristic frequencies of the flow-acoustic feedback. n = 1, 2, … are the mode numbers. α = 0.25 is an empirical constant, and κ = 0.57 is another semi-empirical constant, which is the ratio of the convection velocity of the shear layer U_v to the incoming flow velocity U_∞. L is the length of the cavity. Ma is the ratio of the incoming flow velocity U_∞ to the sound speed c_0.

3.2. Acoustic resonance

The acoustic resonance noise is generated by the acoustic standing wave mode of the cavity. Unlike the flow-acoustic feedback mechanism, which generally exists in the cavity

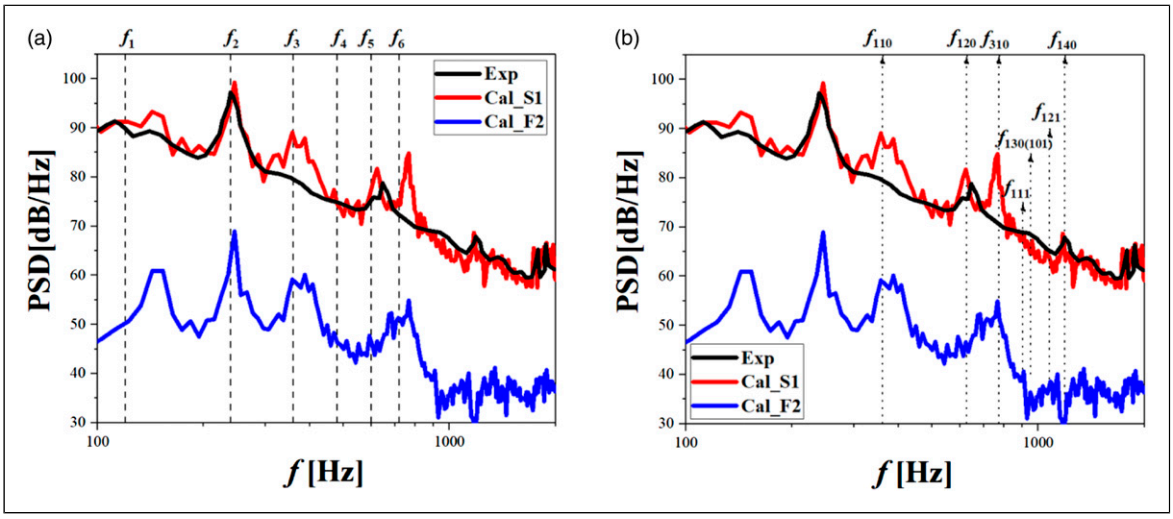

Figure 6. Noise spectra of base case at Ma = 0.16. (a) Dashed lines represent the frequencies predicted by equation (1); Dot lines represent the frequencies predicted by equation (2).

structure, the acoustic resonance mechanism is only common in the deep cavity (L/D <1).

The turbulent disturbance in the shear layer of the cavity mouth, as a random noise source, produces broadband noises. When the sound waves propagate in the cavity, they cause pulsations through the resonance wave effect. According to the size of the cavity, the flow pulsations form several standing waves in the depth-wise, span-wise, and length-wise, respectively, thus amplifying the noise amplitude at certain specific frequencies to form narrowband noises. Because the phenomenon of the acoustic resonance is a pure acoustic phenomenon, the frequencies of these narrowband noises are only related to the geometrical size of the cavity and have no relation to the incoming flow velocity, and can be regarded as the natural frequencies of the cavity.

Ahuja KK et al. (1995) proposed a formula for predicting the characteristic frequencies of acoustic resonance in a square cavity by solving the wave equation with the solid wall of the cavity as the boundary condition, as shown in equation (2).

$$f_{jmn} = \frac{c_0}{2} \cdot \sqrt{\left(\frac{j}{2D}\right)^2 + \left(\frac{m}{W}\right)^2 + \left(\frac{n}{L}\right)^2} \qquad (2)$$

where f_{jmn} are characteristic frequencies of the acoustic resonance, j = 1, 3, 5,…, m = 0, 1, 2, … and n = 0, 1, 2,… are the mode numbers for the depth-wise, span-wise, and length-wise, respectively. D, W, and L are the depth, width, and length of the cavity, respectively. c_0 is the sound speed in the air, 348.91 m/s in this paper.

4. Results and discussion

4.1. Computational results of Base case

According to Guo et al., 2021 explanation of the narrowband noise of the cavity model (the Base case in this paper),

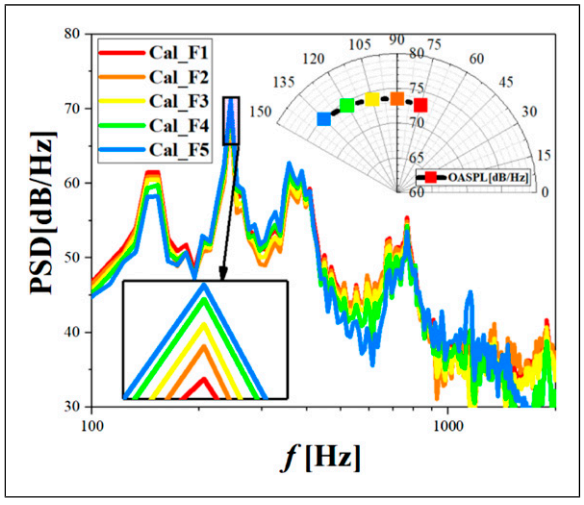

Figure 7. Far-field noise characteristics of base case at different direction angles.

the low-frequency narrowband noise is mainly caused by the flow-acoustic feedback mechanism in the cavity, while the medium-frequency and high-frequency narrowband noises are caused by the acoustic resonance mechanism. Therefore, the noise spectrum results of the Base case at Ma = 0.16 are compared with the predicted values of equation (1) and equation (2), respectively, as shown in Figure 6. The black lines represent the experimental results measured at the same position of the surface pressure monitoring point (S1) in this paper. The red lines represent the numerical simulation results of the surface pressure monitoring point (S1), and the blue lines represent the numerical simulation results of the far-field pressure monitoring point (F2). Figure 6(a) compares the frequencies predicted by equation (1) with the noise spectra, and

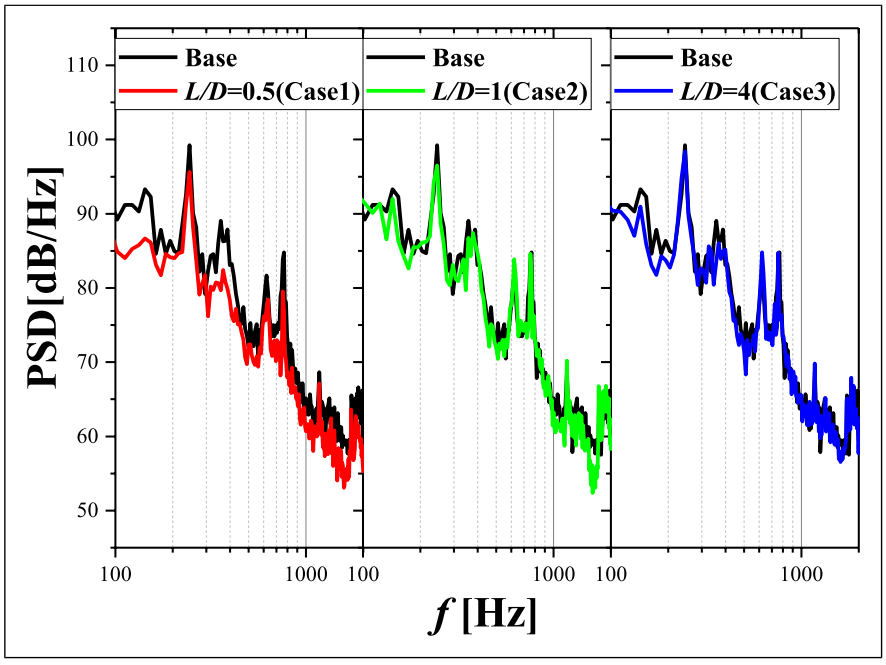

Figure 8. Surface noise spectra of all cases.

Figure 6(b) compares the frequencies predicted by equation (2) with the noise spectra.

It can be seen from the black and red curves that the characteristic frequencies of the narrowband noises between 200 Hz and 700 Hz almost coincide with the characteristic frequencies of the second to sixth modes of flow-acoustic feedback noise predicted by equation (1). The characteristic frequencies of some narrowband noises between 300 Hz and 700 Hz are also in good agreement with the characteristic frequencies of acoustic resonance noise predicted by equation (2), especially the tones near 600 Hz and 700 Hz, whose characteristic frequencies are more consistent with the prediction result of equation (2), compared with that of equation (1). Between 300 Hz and 700 Hz, the characteristic frequencies of the two noise mechanisms are highly coincident, and the coupling of the two noise mechanisms amplifies the pressure oscillations, according to the view proposed by Verdugo et al. (2012). The characteristic frequencies of narrowband noises above 700 Hz are in good agreement with the prediction result of equation (2).

It can be seen from the blue curves that only the narrowband noise from 100 Hz to 400 Hz and near 700 Hz can well propagate to the far-field, while other narrowband noises are almost indistinguishable in the far-field noise spectrum. In other words, only the flow-acoustic feedback noises and the coupling noises can propagate to the far-field, while the acoustic resonance noises hardly propagate to the far field.

Figure 7 shows the far-field noise spectrum and the OASPL at the direction angles of 75°, 90°, 105°, 120°, and 135°. The larger the direction angle is, the lower the broadband noise amplitude is, but the stronger the narrowband noise caused by the flow-acoustic feedback mechanism is. This indicates that the main propagation direction of the flow-acoustic feedback noises is towards the upstream of the flow, which indirectly explains why the greater direction angle results in the stronger OASPL.

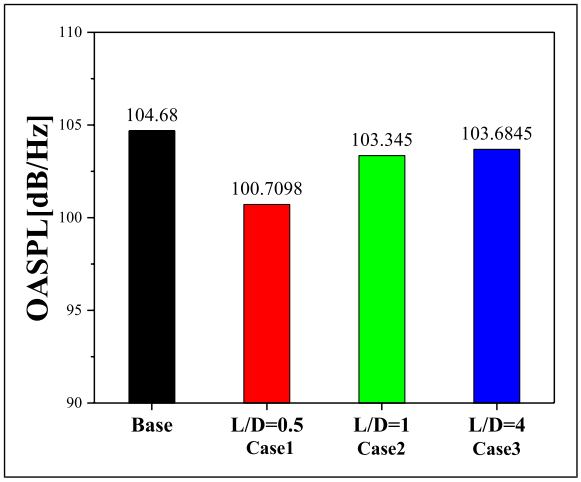

Figure 9. Overall sound pressure level of surface noise of all cases.

4.2. Acoustic analysis of control effect

The effect of noise control of the grooves with different length-to-depth ratios (*L/D*) will be analyzed in this

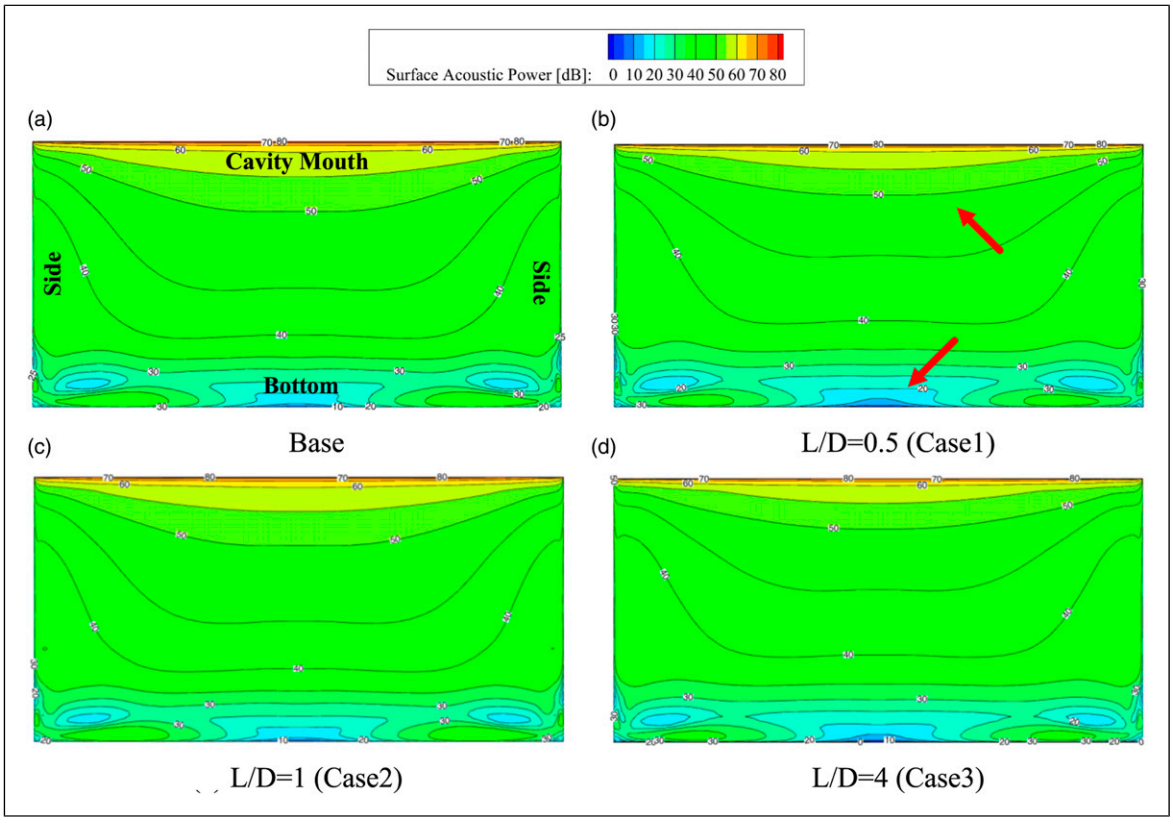

Figure 10. Contour maps of surface acoustic power of rear wall. (a) Base; (b) L/D = 0.5 (Case1); (c) L/D = 1 (Case2); (d) L/D = 4 (Case3).

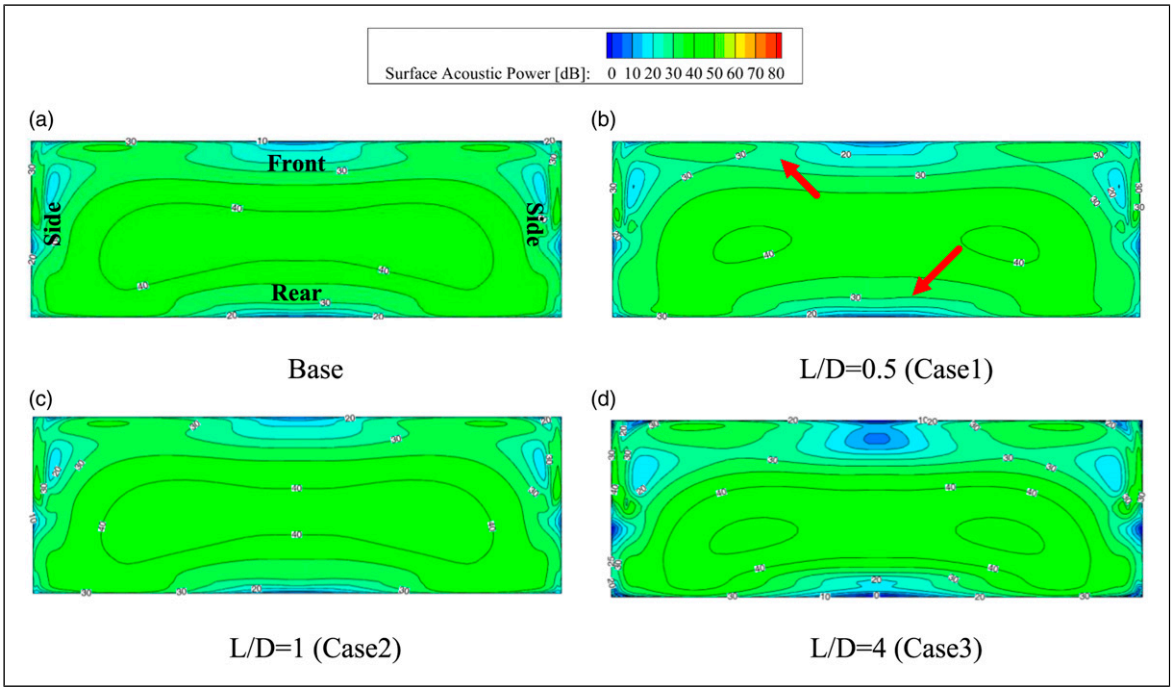

Figure 11. Contour maps of surface acoustic power of bottom wall. (a) Base; (b) L/D = 0.5 (Case1); (c) L/D = 1 (Case2); (d) L/D = 4 (Case3).

subsection. The analyzed frequency range is from 100 Hz to 2000 Hz.

Figure 8 shows the surface noise spectra of three leading-edge grooves with different depths and that of the Base case. The black curve represents the noise spectrum of the Base case, and the red, green, and blue curves represent the spectrum of the grooves with L/D of 0.5, 1, and 4, respectively.

It can be seen from Figure 8 that these three grooves all have a certain noise control effect, and the groove with the most obvious noise reduction is the one with a length-to-depth ratio of 0.5, namely, the deep groove. It can also be seen from the comparison of the black and red curves that the presence of the deep groove significantly suppresses the broadband noise on the cavity surface, as well as the narrowband noise generated by the flow-acoustic feedback and the acoustic resonance mechanism. Compared with the deep groove, the noise reduction effects of grooves with L/D of 1 (square groove) and 4 (shallow groove) are slightly worse. The noise reduction effects of these two grooves are similar, and there is almost no noise reduction on the broadband noise and the narrowband noise generated by the acoustic resonance mechanism. But there is a little noise reduction effect on the narrowband noise generated by the flow-acoustic feedback mechanism.

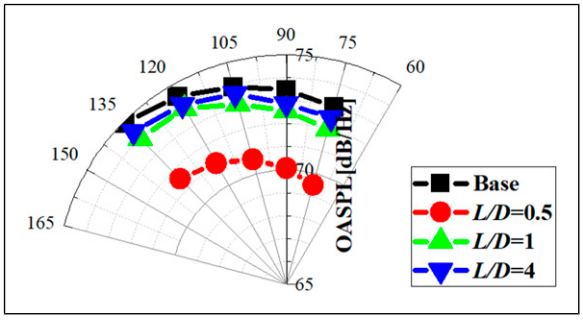

Figure 12. Overall sound pressure level of far-field noise at different direction angles.

Figure 9 shows the OASPL of surface noise of all cases. As shown in Figure 9, for the Base case where there is no groove for flow and noise control, the OASPL of surface noise is 104.68 dB/Hz, while the OASPL decreases after the grooves in front of the cavity are used for flow and noise control. The groove with the most obvious noise reduction effect is the deep groove, which reduces the OASPL by 3.9 dB/Hz. The square groove and the shallow groove also have noise reduction effects, but not obvious. The total sound pressure level is reduced by about 1 dB/Hz. The results of Figure 9 further confirm the conclusions in Figure 8.

Figures 10 and 11 show the contour maps of surface acoustic power of rear and bottom walls of the cavity, respectively. It can be seen from Figure 10 that the presence of the deep and shallow grooves results in a small reduction in the surface acoustic power at the rear wall of the cavity mouth and bottom (as shown by the red arrows) compared to the Base case. It can be seen from Figure 11 that the presence of the deep groove results in

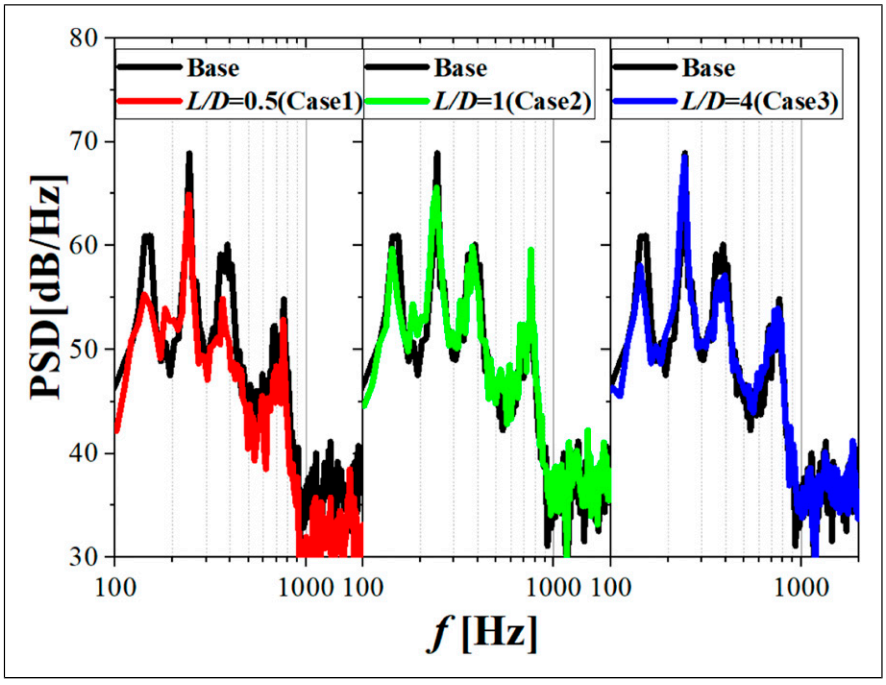

Figure 13. Far-field noise spectra at the direction angle of 90°.

a reduction in the surface acoustic power at the cavity bottom, whether at the front, rear, or center of the cavity bottom. However, the presence of the shallow groove significantly reduces the surface acoustic power at the front and rear edges of the cavity bottom, but slightly increases the noise at the center of the cavity bottom. The presence of the square groove hardly changes the characteristics of the surface acoustic power at the rear and bottom walls.

Figure 12 shows the OASPL at the direction angles of 75°, 90°, 105°, 120°, and 135°. Figure 13 shows the far-field noise spectra at the direction angle of 90°. It shows that the OASPL and spectral results of far-field noise are consistent with those of surface noise. Due to the presence of the leading-edge deep groove, both narrowband noise and broadband noise significantly reduce, and the OASPL reduces by about 4dB. The other two grooves also have a little noise reduction effect.

4.3. Flow control mechanism

As is mentioned in Section 3, the aerodynamic noise characteristics of the cavity are closely related to the flow characteristics near the cavity, especially the cavity mouth. To further study the noise reduction effect and flow control mechanism of the leading-edge grooves, the flow field characteristics of the boundary/shear layer near the cavity mouth and within the cavity will be analyzed in this section.

Figure 14 shows the velocity characteristic of the boundary layer at the front-edge of the cavity mouth. It can

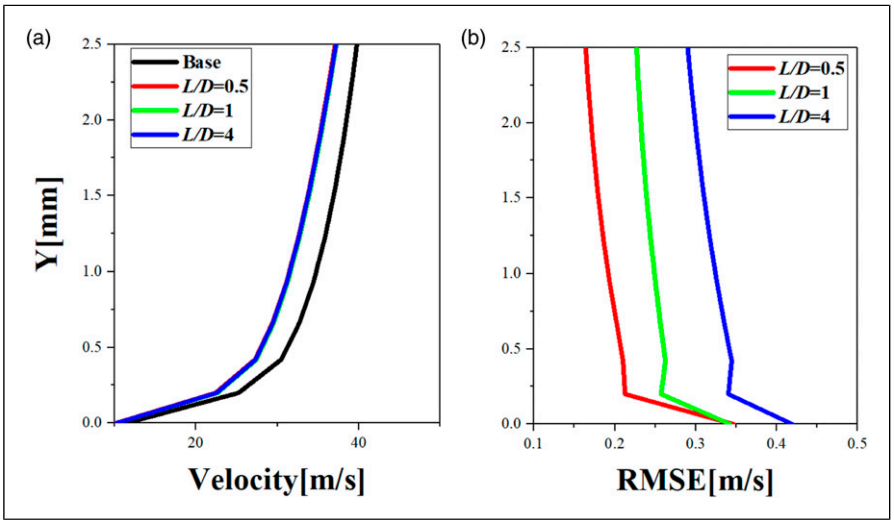

Figure 14. Velocity characteristic of the boundary layer at the front-edge of the cavity mouth. (a) Time-averaged flow velocity distribution of the boundary layer at the front-edge of the cavity mouth. (b) Root mean square error of the velocity of the boundary layer at the front-edge of the cavity mouth.

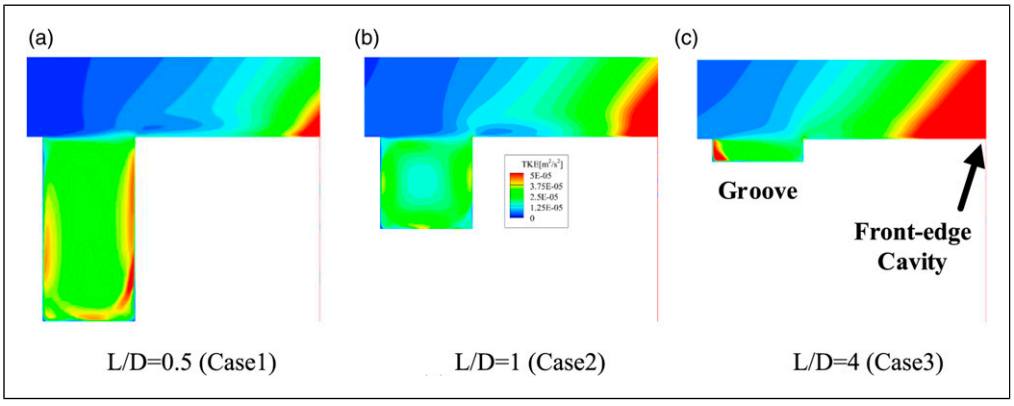

Figure 15. Contour maps of turbulent kinetic energy (TKE) of the groove. (a) L/D = 0.5 (Case1); (b) L/D = 1 (Case2); (c) L/D = 4 (Case3).

be seen from Figure 14(a) that except for the Base case, the velocity profiles of the boundary layer of the other three cases with the grooves almost coincide, which indicates that the time-averaged flow velocities in the boundary layer of these three cases are almost constant. Compared with the Base case, the presence of the grooves reduces the incoming flow velocity of the boundary layer of the cavity. In addition, Figure 14(b) shows the root mean square error (RMSE) of the velocity of the cases with the grooves. It can be seen that the fluctuation of the velocity in the boundary layer increases as the depth of the groove decreases. This indicates that the smaller the groove depth is, the stronger the energy pulsation is, although the energy in the incoming boundary layer is consistent. The deeper grooves make the flow more stable.

Figure 15 shows the contour maps of turbulent kinetic energy (TKE) of the groove. For the deep groove, most of the TKE in the incoming flow enters the interior along the groove wall as the air flows through it. There is also some TKE that goes downstream, and the shallower the groove, the stronger the TKE downstream of the groove. Therefore, the TKE at the mouth of the deep groove and the wall

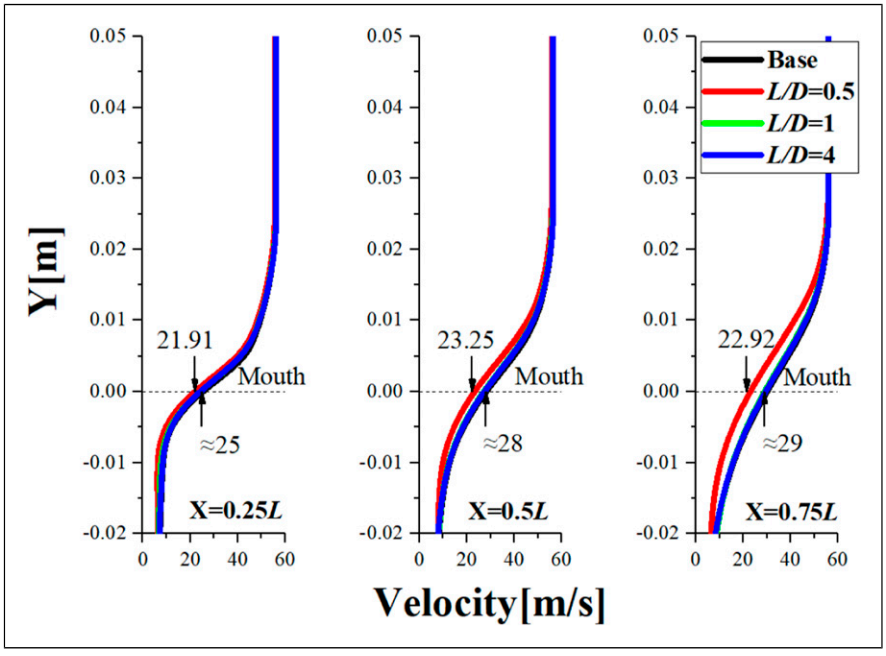

Figure 16. Time-averaged flow velocity distribution of the shear layers on the cavity mouth.

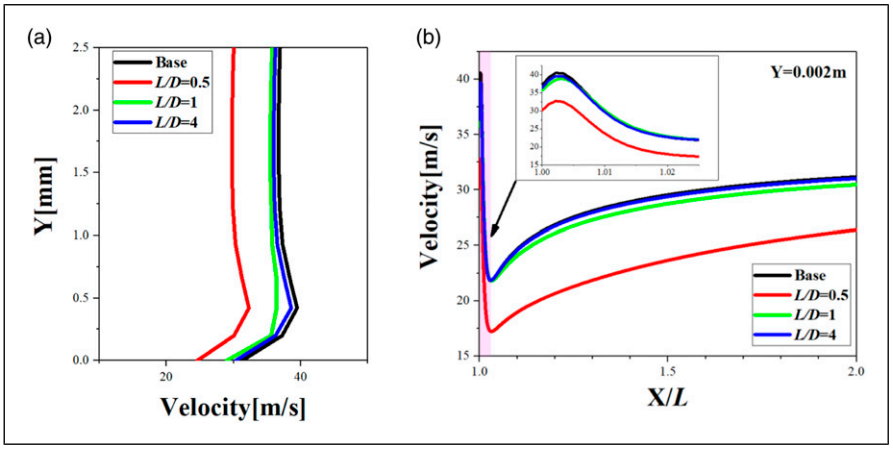

Figure 17. Velocity characteristic of the boundary layer near the rear-edge of the cavity mouth. (a) Time-averaged flow velocity distribution of the boundary layer at the rear-edge of the cavity mouth. (b) Time-averaged flow velocity distribution along the development direction of boundary layer at the rear-edge wall surface.

between the groove and the cavity is significantly lower than in the other two cases.

Figure 16 shows the time-averaged velocity distribution of the shear layers at X/L = 0.25, 0.5, and 0.75 on the cavity mouth. Due to the shear effect, the energy of the fluid outside the shear layer gradually transfers to the inside of the shear layer during the development of the shear layer, which accelerates the flow on the cavity mouth along the development direction of the shear layer. It can be seen that the black, green, and blue lines almost coincide, indicating that the convective velocities in the shear layer are almost equal for these three cases. Compared with the Base case and the cases with the square and shallow grooves, the value of the case with the deep groove (red curve) is smaller, in which the flow acceleration of the shear layer is not obvious. At x = 0.75 L, the convective velocity of the shear layer decreases slightly. Therefore, the deep groove in front of the cavity reduces the energy variation of the shear layer flow and stabilizes the shear layer flow on the cavity mouth.

Figure 17(a) shows the time-averaged flow velocity distribution of the boundary layer at the rear-edge of the cavity mouth. At the rear-edge of the cavity mouth, the flow velocity of the case with deep groove is obviously lower than that of other case. Compared to the results of the Base case, there is a slight reduction in the flow velocity for the shallow and square groove cases. Figure 17(b) shows the time-averaged velocity distribution along the development direction of boundary layer at the rear-edge wall surface. The variation trends of the flow on the rear-edge wall surface are the same for all the cases, with a slight acceleration first, then a sharp deceleration, and finally a slow acceleration till stable. In addition, in the whole process of flow development along the rear-edge wall, the flow velocity of the case with deep groove is obviously lower than that of other case. This further indicates that the control effect of the deep groove on the flow of the cavity mouth is the most obvious, which decreases the flow velocity near the rear-edge of the cavity significantly.

Figure 18 shows the contour maps of time-averaged velocity, and Figure 19 shows the contour maps of TKE. It can be seen from Figure 18(a) and Figure 19(a) that when there is no groove in front of the cavity for flow control, the main vortex structure in the cavity is concentrated at the front-edge near the cavity mouth. The position of the strongest TKE is at the bottom of the rear-edge of the cavity, followed by the position near the rear-edge of the cavity mouth and the concentration position of the vortex structure.

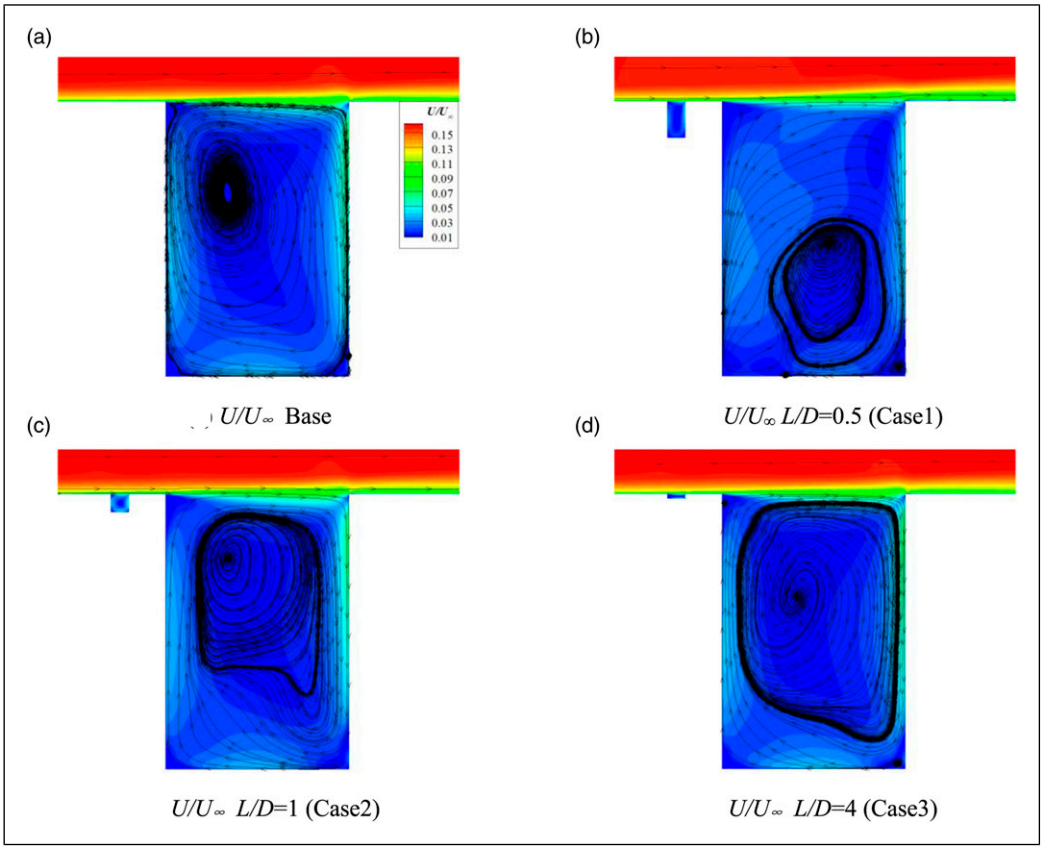

Figure 18. Contour maps of time-averaged velocity. (a) U/U_∞ Base; (b) U/U_∞ L/D = 0.5 (Case1); (c) U/U_∞ L/D = 1 (Case2); (d) U/U_∞ L/D = 4 (Case3).

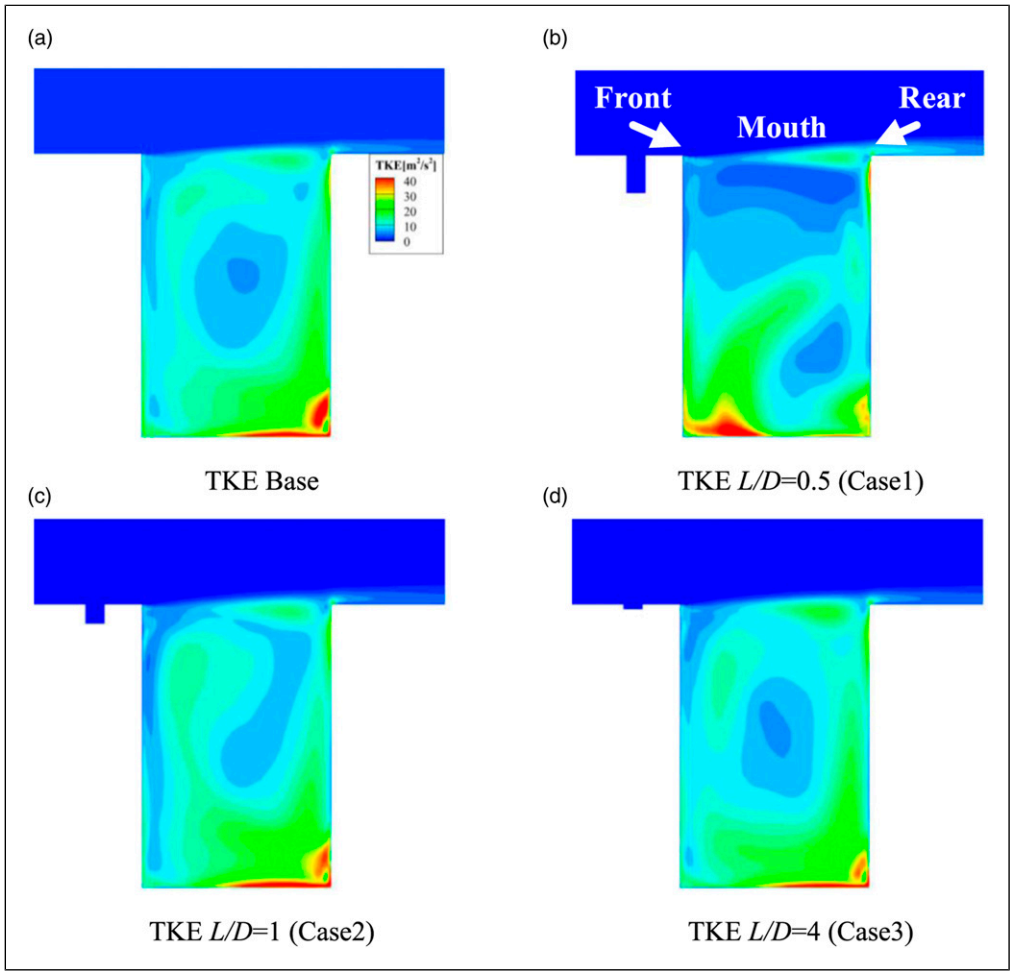

Figure 19. Contour maps of turbulent kinetic energy of the cavity. (a) TKE Base; (b) TKE *L*/*D* = 0.5 (Case1); (c) TKE *L*/*D* = 1 (Case2); (d) TKE *L*/*D* = 4 (Case3).

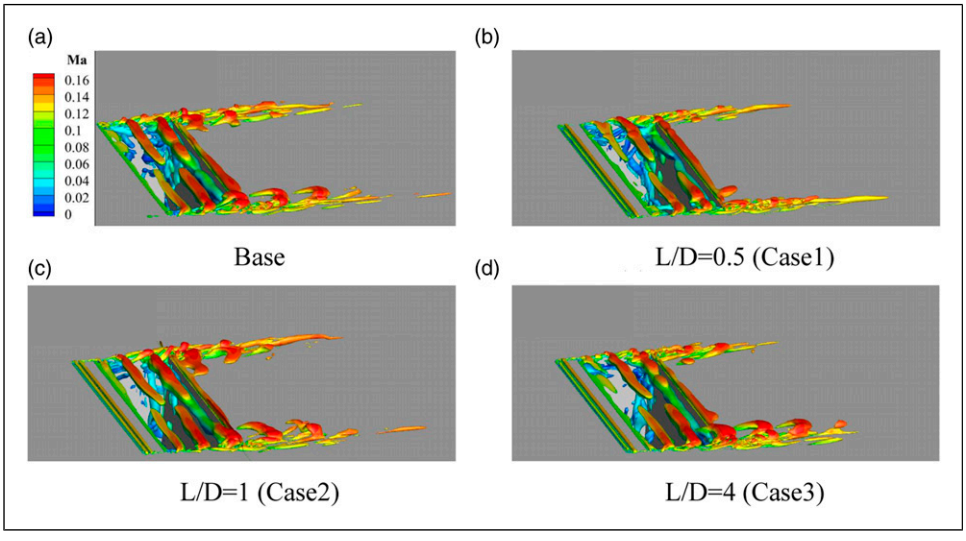

Figure 20. Instantaneous iso-surface of Q criteria colored by the Mach number. (a) Base; (b) L/D = 0.5 (Case1); (c) L/D = 1 (Case2); (d) L/D = 4 (Case3).

Compared with the Base case, the vortex concentration position in the cavity moves obviously to the bottom of the rear-edge of the cavity when the deep groove is used for flow control, as shown in Figure 18(b). In addition, as shown in Figure 19(b), the energy of the shear layer near the cavity mouth, rear-edge of the cavity wall, and rear-edge of the cavity bottom decreases obviously, while the TKE at the front and rear edge of the cavity mouth, the front-edge of the cavity bottom increases obviously. The deep groove at the upstream pushes the energy in the shear layer of the downstream cavity towards the front-edge as well as the bottom of the cavity.

Compared with the deep groove case, the flow controls using a square groove and a shallow groove have less influence on the flow characteristics in the downstream cavity, and there is no significant change in the vortex concentration position and the TKE distribution in the cavity.

To get further information of the characteristics of the cavity flow, Figure 20 shows the instantaneous iso-surface of Q criteria colored by the Mach number. For the four cases studied in this paper, the flow structures near the cavity mouth and within the cavity are similar. The shear layers are all characterized by span-wise coherent structures, presenting the behavior of vortex shedding from the leading edge of the cavity. The coherence is kept until the shear layer hits the rear wall. However, compared to the results in the other three subfigures, the size of the vortices in the cavity shear layer in Figure 20(b) is slightly smaller and the Ma number is reduced. These indicate that the leading-edge grooves does not disrupt the vortex structure of the cavity shear layer, but rather reduce its strength, especially the deep grooves.

5. Conclusion

The noise characteristics of the deep cavity following leading-edge grooves with different length-to-depth ratios have been investigated numerically in this paper. The length-to-depth ratios of these grooves are 0.5, 1, and 4, respectively. The length-to-depth ratio of the deep cavity is 2/3. The purpose was to analyze the noise control effect of the leading-edge grooves and its flow mechanism. The DES combined with Ffowcs Williams–Hawkings (FW-H) acoustic analogy were adopted to simulate the flow and noise characteristics of the cavities. The results have shown the following:

By analyzing the far-field and surface noise results of the Base case (without the grooves for noise control), it is found that, the low-frequency (100–700 Hz) narrowband noise is mainly caused by the flow-acoustic feedback mechanism in the cavity, while the medium-frequency and high-frequency (above 300 Hz) narrowband noises are caused by the acoustic resonance mechanism. Only the flow-acoustic feedback noises and the coupling noises can propagate to the far-field, while the acoustic resonance noises hardly propagate to the far field.

All grooves investigated in this paper have a certain noise control effect, and the case with the most obvious noise reduction effect is the groove with a length-to-depth ratio of 0.5, namely, the deep groove. Due to the presence of the leading-edge deep groove, the narrowband noise generated by the flow-acoustic feedback and the acoustic resonance mechanism and broadband noise caused by the turbulent disturbance in the shear layer of the cavity mouth significantly reduce, and the OASPL lowers by about 4dB. The other two grooves also have some noise reduction effect, but obvious. There is almost no noise reduction effect on the broadband noise and the narrowband noise generated by the acoustic resonance mechanism, yet there is a little noise reduction effect on the narrowband noise generated by the flow-acoustic feedback mechanism.

Compared to the Base case, the presence of the deep groove result in a small reduction in the surface acoustic power at the rear wall of the cavity mouth and at the cavity bottom. The presence of the shallow groove significantly reduces the surface acoustic power at the rear wall of the cavity mouth, the front and rear edges of the cavity bottom, but slightly increases the noise at the center of the cavity bottom. The presence of the square groove hardly changes the characteristics of the surface acoustic power at the rear and bottom walls.

Based on the further analysis of the flow mechanism of noise controls, it is found that the leading-edge grooves can effectively change the flow characteristics near the mouth of the downstream cavity. The energy in the boundary layer of the incoming flow of the cavity significantly reduced when the grooves were used for control, and the control of the deep groove pushes most of the TKE in the incoming flow into the interior along the groove wall and suppress the velocity of the incoming flow of the cavity. The control also promotes the vortex concentration position to move towards the bottom of the cavity, and pushes the energy in the shear layer of the downstream cavity towards the front-edge as well as the bottom of the cavity. However, leading-edge grooves do not alter the flow structure of the shear layers, which are all characterized by span-wise coherent structures, presenting the behavior of vortex shedding from the leading edge of the cavity. The coherence is kept until the shear layer hits the rear wall.

Declaration of conflicting interests

The author(s) declared no potential conflicts of interest with respect to the research, authorship, and/or publication of this article.

Funding

The author(s) disclosed receipt of the following financial support for the research, authorship, and/or publication of this article: This work was supported by the Postdoctoral Fund of Chinese Academy of Sciences (Grant No. E2XM0404).

ORCID iD

Guannan Zheng https://orcid.org/0000-0003-4384-3131

References

Abdelmwgoud M, Shaaban M and Mohany A (2020) Flow dynamics and azimuthal behavior of the self-excited acoustic modes in axisymmetric shallow cavities. *Physics of Fluids* 32(11), 115109(2020).

Ahuja KK and Mendoza J (1995) *Effects of Cavity Dimensions, Boundary Layer, and Temperature on Cavity Noise with Emphasis on Benchmark Data to Validate Computational Aeroacoustic Codes*. NASA Contractor Report 4653.

Casalino D, Ribeiro AFP and Fares E (2014) Facing rim cavities fluctuation modes. *Journal of Sound and Vibration* 333(13): 2812–2830.

Chen GY, Tang XL, Yang XQ, et al. (2021) Noise control for high-lift devices by slat wall treatment. *Aerospace Science and Technology* 115(2021): 106820.

Chaudhari K and Raman G (2011) Control of flow over a rectangular cavity using a rod in cross flow: further evaluation of key mechanisms, In: Proceedings of the 49th AIAA Aerospace Sciences Meeting including the New Horizons Forum and Aerospace Exposition, Orlando, Florida, 4-7 January 2011. FL: American Institute of Aeronautics and Astronautics.

Dobrzynski W (2010) Almost 40 Years of airframe noise research: what did we achieve? *Journal of Aircraft* 47(2): 353–367.

East LF (1966) Aerodynamically induced resonance in rectangular cavities. *Journal of Sound and Vibration* 3(3): 277–287.

Guo Z, Liu P and Gou H (2021) Control effect on deep cavity noise by slanted walls at low Mach numbers. *Journal of Vibration and Control* 27(9–10): 998–1008.

Lawson SJ and Barakos GN (2009) Assessment of passive flow control for transonic cavity flow using detached-eddy simulation. *Journal of Aircraft* 46(3): 1009–1029.

Li Y, Wang XN and Zhang DJ (2013) Control strategies for aircraft airframe noise reduction. *Chinese Journal of Aeronautics* 026(002): 249–260.

Mendoza JM (1997) *Effects of Cavity Dimensions, Boundary Layer, and Temperature on Cavity Noise Generation and Control*. Atlanta, GA: Georgia Institute of Technology. Report no.:4948.

Pereira L, Catalano F, Almeida O, et al. (2021) Feasibility of measuring noise sources on a detailed nose landing gear at low cost development. *Applied Acoustics* 182(2021): 108263.

Pott-Pollenske M, Dobrzynski W, Buchholz H, et al. (2002) Validation of a semiempirical airframe noise prediction method through dedicated A319 flyover noise measurements. In: Proceedings of the 8th AIAA/CEAS aeroacoustics conference & exhibit, Breck-enridge, 17 June 2002, Breckenridge: American Institute of Aeronautics and Astronautics, p. 2470.

Rockwell D and Naudascher E (1978) Review: self-sustaining Oscillations of flow past cavities. *Journal of Fluids Engineering, Transactions of the ASME* 100(2): 152–165.

Rossiter JE (1964) *Wind Tunnel Experiments on the Flow over Rectangular Cavities at Subsonic and Transonic Speeds*. Technical Report, Report no.: 64037. Netherlands: Ministry of Aviation; Royal Aircraft Establishment.

Saddington AJ, Thangamani V and Knowles K (2016) Comparison of passive flow control methods for a cavity in transonic flow. *Journal of Aircraft* 53(5): 1439–1447.

Taborda N, Bray D and Knowles K (2001) Experimental investigation into transonic flows over tandem cavities. *Aeronautical Journal* 105(1045): 119–124.

Verdugo FR, Guitton A and Camussi R (2012) Experimental investigation of a cylindrical cavity in a low Mach number flow. *Journal of Fluids and Structures* 28: 1–19.

Wang P, Deng Y and Liu Y (2020) Phase-locking particle image velocimetry measurements of acoustic-driven flow interactions between tandem deep cavities. *Physics of Fluids* 32(32): 125115.

Wang Y, Li S and Yang X (2016) Numerical investigation of the passive control of cavity flow oscillations by a dimpled non-smooth surface. *Applied Acoustics* 111(OCT): 16–24.

Zhao K, Okolo P, Neri E, et al. (2020). Noise reduction technologies for aircraft landing gear-A bibliographic review. *Progress in Aerospace Sciences*. 112(2020):100589.

Zhang X and Edwards JA (1992) Experimental investigation of supersonic flow over two cavities in tandem. *AIAA Journal* 30(5): 1182–1190.

Zhang X and Edwards JA (1999) Pressure over a dual-cavity cascade at supersonic speeds. *Aeronautical Journal* 103(1019): 45–54.